DTU Library

Engineering covalently bonded 2D layered materials by self-intercalation

Zhao, Xiaoxu; Song, Peng; Wang, Chengcai; Riis-Jensen, Anders Christian; Fu, Wei; Deng, Ya; Wan, Dongyang; Kang, Lixing; Ning, Shoucong; Dan, Jiadong

Total number of authors:
17

Citation (APA):
Zhao, X., Song, P., Wang, C., Riis-Jensen, A. C., Fu, W., Deng, Y., Wan, D., Kang, L., Ning, S., Dan, J., Venkatesan, T., Liu, Z., Zhou, W., Thygesen, K. S., Luo, X., Pennycook, S. J., & Loh, K. P. (2020). Engineering covalently bonded 2D layered materials by self-intercalation. *Nature*, *581*(7807), 171-177. https://doi.org/10.1038/s41586-020-2241-9

Engineering Covalently Bonded 2D Layered Materials by Self-Intercalation

Xiaoxu Zhao[1,2], Peng Song[2], Chengcai Wang[3], Anders C. Riis-Jensen[4], Wei Fu[2], Ya Deng[5], Dongyang Wan[6], Lixing Kang[5], Shoucong Ning[1], Jiadong Dan[1], T. Venkatesan[1,6], Zheng Liu[5], Wu Zhou[7], Kristian S. Thygesen[4], Xin Luo[8*], Stephen J. Pennycook[1*], and Kian Ping Loh[2*]

[1]Department of Materials Science and Engineering, National University of Singapore, 9 Engineering Drive 1, 117575, Singapore

[2]Department of Chemistry and Centre for Advanced 2D Materials, National University of Singapore, 3 Science Drive 3, Singapore, 117543, Singapore

[3]Department of Electrical and Electronic Engineering, Southern University of Science and Technology, Shenzhen, 518055, China

[4]CAMD and Center for Nanostructured Graphene (CNG), Department of Physics, Technical University of Denmark, DK-2800 Kongens Lyngby, Denmark

[5]School of Materials Science and Engineering, Nanyang Technological University, Singapore, 639798, Singapore

[6]NUSNNI-NanoCore, National University of Singapore, Singapore 117411

[7]School of Physical Sciences and CAS Centre for Excellence in Topological Quantum Computation, University of Chinese Academy of Sciences, Beijing 100049, China

[8]State Key Laboratory of Optoelectronic Materials and Technologies, Centre of Physical Mechanics and Biophysics, Sun Yat-sen University, Guangzhou 510275, China

Correspondence and requests for materials should be addressed to X. L. (luox77@mail.sysu.edu.cn) S. J. P (steve.pennycook@nus.edu.sg) & K. P. L (chmlohkp@nus.edu.sg)

X. Zhao & P. Song contributed equally to this work

Abstract:

Two-dimensional (2D) materials[1–5] offer a unique platform for exploring the physics of topology and many-body phenomena. Filling the van der Waals (vdW) gap of 2D materials with intercalants is expected to create new properties[6,7], but post-growth intercalation is usually limited to alkali metals[8–10]. Here, we show that self-intercalation of native atoms[11,12] into bilayer transition metal

dichalcogenides (TMDs) during growth creates a whole new class of ultrathin, covalently bonded materials (named *ic*-2d). The stoichiometry of *ic*-2d is defined by periodic occupancy patterns of the octahedral vacancy sites in the vdW gap, and its properties can be tuned by varying the coverage and spatial arrangement of the filled sites[7,13]. By performing growth under conditions of high metal chemical potential[14,15], we can grow a full spectrum of Ta-intercalated TaS(Se)$_y$, including 25% intercalated Ta$_9$S$_{16}$, 33.3% intercalated Ta$_7$S$_{12}$, 50% Ta$_{10}$S$_{16}$, 66.7% Ta$_8$Se$_{12}$ (Kagome lattice) and 100% Ta$_9$Se$_{12}$. Ferromagnetic order was detected for some of the intercalated phases. We have also verified that self-intercalated V$_{11}$S$_{16}$, In$_{11}$Se$_{16}$, and Fe$_x$Te$_y$, can be grown under metal-rich conditions. Our work establishes self-intercalation as a novel approach to grow a new class of *ic*-2d materials with stoichiometry or composition-dependent properties.

Introduction

The surge in 2D materials research has heralded a new branch of condensed-matter physics concerned with the description of electrons in atomically thin structures. Thus far, research efforts have primarily focused on 2D monolayers[2] and their hetero-stacked structures[3], in which new properties can be engineered by generating superlattices of different Moiré wavelengths. However, these hetero-stacked structures are currently produced by bottom-up methods that have low yield and poor reproducibility[16]. An alternative way of compositional tuning is based on the intercalation of foreign atoms in the vdW gap sandwiched by the chalcogen atoms; this has been shown to induce pseudo-2D characteristics in bulk crystals and modify their electronic properties[4,6,7]. Depending on the interlayer stacking registries, the vdW gaps in TMDs contain octahedral and tetrahedral vacancies or trigonal-prismatic vacancies[13], which provide docking sites for a diverse range of intercalants. Examples of successful intercalants include alkali metals[8–10] such as Li, Na, K; transition metals[17–21] such as Cu, Co, Ni, Fe, Nb, Sn; noble metals[22–24] such as Ag, Au, Pt; and various organic molecules[25–27]. Charge transfer from the intercalants[7], or increased spin-

53 orbit coupling owing to the presence of heavy atoms[7,24,28], can enhance superconductivity[10],

54 thermoelectricity[25], or spin polarization[7]. The intercalation process typically involves post-growth,

55 diffusion-limited processes such as electrochemical or solid-state intercalation. A well-defined

56 intercalated phase with long-range crystalline order is difficult to obtain by such methods and usually

57 requires drastic treatment conditions[29]. Moreover, an intercalation phase diagram that correlates the

58 density and spatial distribution of intercalation atoms with mesoscopic properties of the intercalated

59 compound is currently lacking. Compared with foreign atom intercalation, intercalation of a TMD by its

60 native metal atoms has so far received scant attention[11,29,30]. Such self-intercalated TMD compounds may

61 exist as local energy minima in the part of the phase diagram where a metal-rich stoichiometry is

62 promoted by growth conditions using high chemical potential of metal atoms. However, to date, growth

63 windows of TMDs using high metal chemical potential remain relatively unexplored[31,32].

64 In this work, we studied the growth of 2D TMDs under conditions of high metal chemical potential using

65 both molecular beam epitaxy (MBE) and chemical vapor deposition (CVD). We discovered that

66 independent of the employed growth method, a metal-rich chemical potential promotes the self-

67 intercalation of M into MX, MX_2, or M_2X_3 layered 2D compounds to produce a covalently bonded *ic*-2d

68 M_xX_y compound (M = metal, X = chalcogen). Using TaS_2 as an example, intercalated Ta atoms occupy the

69 octahedral vacancies in the vdW gap to form distinct topographical patterns, as verified by the atomic

70 resolution scanning transmission electron microscopy − annular dark field (STEM–ADF) imaging. By

71 varying the ratio of intercalated atoms to the octahedral vacancies in the vdW gap, we were able to grow

72 Ta_xS_y or Ta_xSe_y films with σ% of Ta-intercalation, where σ% refers to the ratio of occupied vacancy sites to

73 the initial total vacancy sites. Our results indicate that self-intercalation is generic to a broad class of vdW

74 crystals and it offers a powerful approach to transform layered 2D materials into ultrathin, covalently

75 bonded *ic*-2d crystals with ferromagnetic properties.

76   **Results and discussion:**

77   We first describe the self-intercalation of a TaS_2 bilayer by native atoms (*i.e.,* Ta) during MBE deposition

78   on a silicon wafer, this is used as an example to demonstrate the transformation of a 2D bilayer film into

79   an *ic*-2d film *via* octahedral vacancy filling. Wafer-scale Ta-intercalated TaS_2 bilayer films were grown on

80   2-inch 285 nm SiO_2/Si wafers in a dedicated MBE system[14]. Ultra-pure Ta and S molecular beams were

81   evaporated from an e-beam evaporator and sulfur cracker cell equipped with a valve, respectively (Fig.

82   1a-b). We can routinely grow 2H-phase TaS_2 bilayer films using a high S chemical potential, *i.e.,* Ta to S

83   flux ratio ~1:10 (Fig. 1a and Supplementary Fig. 1) for 3 hours, and a substrate temperature of 600 °C.

84   When the Ta:S flux ratio was increased to 1:6 (Fig. 1c), the film became non-stoichiometric with respect

85   to TaS_2 owing to the excess Ta atoms. A fingerprint of the Ta-rich environment is the presence of Ta

86   adatoms (Fig. 1d) occupying the center of the honeycombs (highlighted in yellow) (Fig 1e) or atop of the

87   Ta sites (highlighted in white) (Fig. 1f) in monolayer TaS_2 film, as observed by STEM when the growth was

88   interrupted mid-way (Supplementary Fig. 2). By continually supplying Ta and S in the requisite ratio, the

89   Ta adatoms become embedded and occupy the octahedral vacancies between two S layers (Fig. 1g).

90   Therefore, the growth mechanism of *ic*-2d crystals follows a sequential TaS_2-Ta-TaS_2-Ta layer-by-layer

91   growth, such that multilayer or bulk phase *ic*-2d crystals can be readily accessed by simply increasing the

92   growth time. The thermodynamic stability of such intercalated phases is analyzed by the energy-

93   composition phase diagram generated through our DFT calculations (Fig. 1h).It can be seen that

94   stoichiometric H-phase TaS_2 is only formed under S rich conditions (μ_S > -5.3 eV), whereas under low μ_S,

95   various Ta-intercalated Ta_xS_y configurations, ranging from Ta_9S_{16} (33.3% Ta intercalation) to Ta_9S_{12} (100%

96   Ta intercalation), entered a thermodynamically stable state.

97   Notably, a ~1:6 Ta:S ratio in the beam flux produced a $\sqrt{3}a \times \sqrt{3}a$ superlattice of Ta atoms (Fig. 2a)

98   sandwiched between two TaS_2 monolayers. The coverage σ was 33.3%, and the overall stoichiometry of

99   the crystal thus became Ta_7S_{12}, as corroborated by both the real space STEM image (Fig. 2b) and the

100 corresponding fast Fourier transform (FFT) pattern (Fig. 2c). Image simulation and sequential STEM images

101 capturing the diffusion of intercalated atoms proved that the periodically arranged bright spots in the

102 STEM image were induced by the Ta intercalation (see Fig. 2d, Supplementary Information section 1, and

103 Supplementary Videos 1-2). We have also collected STEM cross-section image (Fig. 2e-f) to prove the

104 existence of an intercalated Ta atomic layer in the vdW gap of ic-2d films grown by CVD.

105 The homogeneous Ta_7S_{12} phase was grown directly on a 2-inch silicon wafer (Supplementary Fig. 3). The

106 Ta_7S_{12} film was formed by coalescence of nano-domain crystals (~50 nm) separated by mirror twin

107 boundaries or tilted grain boundaries (Supplementary Information section 2). Amorphous islands and gaps

108 seen in the STEM images were due to the poor stability of Ta_xS_y and sample damage during the sample

109 transfer. Energy dispersive x-ray spectroscopy (EDS) and electron energy loss (EEL) spectroscopy

110 (Supplementary Fig. 4) verified that the chemical composition comprised solely of Ta and S with no foreign

111 elements. X-ray photoelectron spectroscopy (XPS) (Supplementary Fig. 5) confirmed that the chemical

112 stoichiometry agrees very well with Ta_7S_{12}. The Raman spectra of the film exhibited two prominent E^3_g

113 and A^3_{1g} peaks at 300 cm^{-1} and 400 cm^{-1}, respectively, matching those of H-phase TaS_2 films. The

114 fingerprint of the intercalation came from a series of minor peaks in the 100 cm^{-1} to 170 cm^{-1} range

115 (Supplementary Fig. 6), which were absent in pure H-phase TaS_2[33] attributed to the covalent bonds

116 between the intercalated Ta atoms and their octahedrally coordinated S atoms (Supplementary Fig. 7).

117 25% Ta-intercalated TaS_2 has a stoichiometry of Ta_9S_{16} and was produced at a slightly lowered Ta chemical

118 potential, corresponding to a ~1:8 Ta:S ratio. The intercalated Ta atoms occupy the octahedral vacancies

119 in every $2a \times \sqrt{3}$ a unit length, and this phase was distinguished by the square symmetry of the

120 intercalated atomic lattice (Fig. 2g, 2k, and Supplementary Fig. 8). When the Ta:S flux ratio was further

121 increased to 1:5, a $Ta_{10}S_{16}$ phase (σ = 50%) was successfully grown (Fig. 2h). The intercalation

122 concentration was determined to be exactly 50% *via* atom counting (Supplementary Fig. 9). Interestingly,

123 this phase is characterized by short-range interconnected atomic chains forming an overall glassy phase.

124 Clear diffusive rings were observed in the proximity of the first order FFT spots (Fig. 2l and Supplementary

125 Fig. 10), confirming the presence of this short-range ordered structure[34]. When we further enhanced the

126 Ta:S flux ratio, the glassy phase was retained, but the short Ta atomic chains became denser until it fully

127 evolved into a complete atomic plane when σ reached ~100% (Supplementary Fig. 11). When the growth

128 condition straddles between two high-symmetry phases, phase separations occur and atomically sharp

129 domain boundaries separating two high-symmetry phases can be clearly seen (Supplementary

130 Information section 3).

131 To verify that *ic*-2d films could be produced by methods other than MBE, we employed CVD to grow self-

132 intercalated Ta_xSe_y crystals by using excess Ta precursors. The crystal domains of Ta-intercalated Ta_xSe_y

133 films grown by CVD are in the micron-sized range, which are significantly larger than the nanosized domain

134 grown by MBE (Supplementary Fig. 12). A typical Ta_8Se_{12} crystal (σ =66.7%) is depicted in Fig. 2i.

135 Interestingly, it reveals a signature Kagome lattice belonging to the P_6 wallpaper symmetry group. A well-

136 defined $\sqrt{3}a \times \sqrt{3}a$ periodic lattice can be unambiguously identified in the atomic-resolution STEM image

137 (Fig. 2m and the simulated image in Supplementary Fig. 13). At even higher Ta chemical potential, Ta_9Se_{12}

138 crystals ($\sigma = 100\%$) were successfully synthesized, arising from the full occupation of the prismatic vacant

139 sites in *AA*-stacked Ta_9Se_{12} (Fig. 2j), as seen in the STEM top view (Fig. 2n) and side view images (Fig. 2e &

140 Supplementary Fig. 14). By precisely controlling the metal:chalcogen ratio during the growth, a full

141 spectrum of Ta-intercalated Ta_xSe_y or Ta_xS_y compounds with intercalation ratio ranging from $\sigma = 25\%$ to

142 over 100% can be grown, as further verified by EDS (Supplementary Fig. 15 & Supplementary Table 1).

143 In the above example, the intercalated Ta atoms were octahedrally coordinated to the S_6 cage as opposed

144 to the trigonal prismatic coordination adopted by pristine TaS_2. Charge transfer from the intercalated Ta

145   atoms to the TaS_2 host layers creates new electron ordering and modified its *d* band splitting. The

146   tunability in this system stems from the fact that the amount of charge transfer is dependent on the

147   intercalation concentration. To investigate if ferromagnetic order was present in the intercalated samples,

148   magneto-transport measurements were carried out on MBE-grown Ta_7S_{12} (σ = 33.3%) with a

149   predominantly $2H_a$ stacking registry (Fig. 3a and Supplementary Fig. 16) with bilayer thickness

150   (Supplementary Fig. 17). Fig. 3c shows the temperature-dependent resistivity, where a non-saturating

151   upturn is observed below 30 K, due to the disorder-induced metal-insulator transition in the

152   polycrystalline sample[35]. Linear magneto-resistance (MR) up to 9 T at low temperature is observed in

153   Ta_7S_{12} (Fig. 3d) due to the density and mobility fluctuations[36]. The anomalous Hall effect (AHE) arises from

154   the interplay of spin-orbit interactions and ferromagnetic order, and is a potentially useful probe of spin

155   polarization. We observed AHE in Ta_7S_{12} on top of the linear ordinary Hall effect (OHE). Fig. 3e shows the

156   nonlinear Hall effect at the proximity of zero magnetic field and linear OHE at high field. While both

157   multiband conduction and AHE contribute to nonlinear Hall effect, the observed linear OHE suggests

158   single carrier conduction (hole) in Ta_7S_{12} and thus excludes multiband transport as the origin of the

159   nonlinear Hall effect[37,38]. The nonlinear Hall effect is thus ascribed to AHE, which stems from

160   ferromagnetism in conductors[39]. After subtracting the linear OHE, anomalous hall resistance up to 0.75 Ω

161   is observed at 1.5 K; it decreases with increasing temperature and vanishes at 10 K in line with Monte

162   Carlo simulation based on Ising model (Supplementary Fig. 18).

163   The effects of self-intercalation on the electrical properties of TMDCs are further tested on the Kagome

164   lattice Ta_8Se_{12} (σ = 66.7%). It was observed that the intercalation of Ta atoms and formation of Kagome

165   lattices stabilize the charge density wave (CDW) states. Temperature dependent Hall signal reveals AHE

166   below 15 K and confirms the ferromagnetic order in Ta_8Se_{12} (Supplementary Fig. 19-20).

167 We performed DFT calculations to gain an understanding of the origin of the magnetization in self-

168 intercalated Ta_7S_{12}. Perfect bilayer $2H_a$-stacked TaS_2 (Supplementary Fig. 21) possesses a non-magnetic

169 ground state. Ferromagnetism can be induced by the double exchange mechanism[40] triggered by the

170 charge transfer from intercalated Ta to pristine TaS_2 (Fig. 3f). When the intercalated Ta adopts a $\sqrt{3}a$ x $\sqrt{3}a$

171 superstructure, six S atoms bond with one intercalated Ta atom to form an octahedral unit in the vdW

172 gap. In contrast, each S atom is shared by three Ta atoms in the pristine TaS_2 layer. This difference in local

173 bonding arrangement induces charge transfer from the octahedral-coordinated intercalated Ta atom to

174 the prismatic-coordinated Ta atom in the TaS_2 layer (Fig. 3f). In the pristine H-phase TaS_2, the Ta d and S

175 p orbitals are well separated in terms of energy, with the states at the Fermi level having mainly Ta d_{z^2}

176 and Ta d_{x^2} characteristics (Supplementary Fig. 21). In Ta_7S_{12} (σ = 33.3%), the intercalated Ta atoms

177 introduce additional spin-split bands across the Fermi level, and a magnetic ground state develops(Fig.

178 3g-h). The magnetic moments are localized on the d orbitals of the intercalated Ta atom, as evidenced by

179 the calculated orbital-resolved spin up and spin down band structures in Fig. 3g and Fig. 3h, respectively.

180 The states at the Fermi level comprise the prismatic-centred Ta d_{z^2} orbitals hybridized with the spin-up

181 band of the $d_{x^2-y^2}$ orbital of the intercalated Ta. However, only the intercalated Ta atoms exhibit a net

182 spin density, as illustrated in Fig. 3i, where the top view spin density isosurface matches the shape of the

183 $d_{x^2-y^2}$ orbital. In addition, the non-magnetic 3a x 3a CDW state of Ta_7S_{12} can be ruled out owing to its

184 relative instability compared to the ferromagnetic state[41].

185 The existence of a magnetic moment correlates with a strong charge transfer between the intercalated

186 Ta and the TaS_2 layers. Strong charge transfer occurs in the dilute Ta-intercalated compound, whereas the

187 charge transfer becomes relatively weak in a heavily intercalated (Fig. 3j) compound in accordance with

188 the calculated charge difference and the variation of Bader charge in the Ta atoms (Supplementary Table

189 2, & Supplementary Fig. 22).

190   To investigate whether the self-intercalation phenomenon occurred for other TMDs, we performed a

191   high-throughput DFT study of 48 different intercalated TMD bilayers using a semi-automated workflow

192   for maximal consistency and veracity[42]. Specifically, we considered TMDs of the transition metals Mo, W,

193   Nb, Ta, Ti, Zr, Hf, V, Cr, Mn, Fe, Co, Ni, Pd, Pt, and Sn, and the chalcogens S, Se, and Te (highlighted in Fig.

194   4a in blue and red, respectively) when σ equals 33.3% or 66.7%. Out of this set of TMDs, we observed that

195   14 bilayer configurations, Ti_8S_{12}, Ti_8Se_{12}, Ti_8Te_{12}, Co_7S_{12}, Co_7Se_{12}, Co_7Te_{12}, Nb_7S_{12}, Nb_7Se_{12}, Nb_7Te_{12}, Mo_7S_{12},

196   Mo_7Se_{12}, Ta_7S_{12}, Ta_7Se_{12}, and Ta_7Te_{12}, (highlighted in Fig. 4a and Supplementary Table 3 for magnetic

197   moment) develop ferromagnetic order upon self-intercalation, whereas their parental MX_2 are

198   nonferromagnetic. Notably, group V and VI TMDs, exhibit strong ferromagnetism after self-intercalation

199   (Fig. 4b). Intrinsic ferromagnetic MX_2 (VX_2, CrX_2, MnX_2, and FeX_2) retain ferromagnetism upon self-

200   intercalation (highlighted in Fig. 4a in orange). Among the 14 types of self-intercalated 2D ferromagnets,

201   the formation energies of 12 of them (the 2 exceptions being MoS_2 and $MoSe_2$) were lower than or similar

202   to those of the non-intercalated materials (Supplementary Fig. 23-24), indicating that self-intercalation is

203   energetically feasible.

204   To validate the theoretical predictions, we attempted to grow a wide variety of *ic*-2d, as highlighted by

205   the triangle in the top left corner in Fig. 4a. Blue triangles indicate that the self-intercalation can be

206   experimentally realized[11,12], whereas gray triangles indicate that intercalation was not be successful under

207   our experimental conditions. We had succeeded to grow several *ic*-2d crystals, namely $V_{11}S_{16}$ (Fig. 4c and

208   Supplementary Fig. 25), $In_{11}Se_{16}$ (Fig. 4d and Supplementary Fig. 26), and Fe_xTe_y (Fig. 4e and

209   Supplementary Fig. 27) by CVD or MBE. Their clear topological features and corresponding FFT patterns

210   are depicted in Fig. 4f-h. The intercalated $V_{11}S_{16}$ revealed a 2a × 2a superstructure, and the intercalation

211   ratio was estimated at 75% (Fig. 4f). $In_{11}Se_{16}$ also showed a 2a × 2a superstructure, but in this case, the

212   intercalated In atoms reveal a signature honeycomb structure (Fig. 4g). The crystal structure of self-

213   intercalated Fe_xTe_y was rather complicated with additional Fe intercalated into the atomic network of the

214   pristine FeTe matrix as interstitials because telluride based TMDs offer the largest spacing between the

215   host atoms[43]. Upon intercalation, the novel Fe_xTe_y phase reveals new symmetries as confirmed by the

216   emergence of superspots in the FFT pattern (Fig. 4h). Similar complex intercalation network has also been

217   observed in V_xTe_y (Supplementary Fig. 28).

218   **Conclusion**

219   We have discovered a robust way to perform composition engineering of a broad class of TMD by self-

220   intercalation with native metal atoms during growth. The main principle is to apply a high chemical

221   potential of metal atoms to provide the driving force for intercalation during growth, thus it should work

222   for most growth methods. The metal intercalants occupy octahedral vacant sites in the vdW gap, and

223   depending on the coverage patterns, distinct stoichiometric phases are produced. High throughput DFT

224   simulations, supported by growth experiments, show that the self-intercalation method is applicable to a

225   large class of 2D layered materials, thus allowing a whole new library of materials with potentially new

226   properties to be created from existing layered materials. Owing to the versatility in composition control,

227   it is possible to tune in one class of materials, properties that can vary from ferromagnetic to non-

228   ferromagnetic, and spin-frustrated Kagome lattices. In particular, ferromagnetic order can be introduced

229   into non-magnetic layered materials *via* the self-intercalation approach, giving rise to a unique topological

230   phase such as ferromagnetic Kagome lattices. The implication of this work is that bilayer TMD (or thicker)

231   can be transformed into ultrathin covalent bonded 3D material, with a stoichiometry that is tuneable by

232   the concentration of the intercalants over a broad range.

233   **References**

234   1.   Chhowalla, M. *et al.* The chemistry of two-dimensional layered transition metal dichalcogenide
235   nanosheets. *Nature Chemistry* **5**, 263–275 (2013).

236   2.   Zhou, J. *et al.* A library of atomically thin metal chalcogenides. *Nature* **556**, 355–359 (2018).

237 3.   Jin, C. *et al.* Ultrafast dynamics in van der Waals heterostructures. *Nature Nanotechnology* **13**,
238   994–1003 (2018).

239 4.   Wang, C. *et al.* Monolayer atomic crystal molecular superlattices. *Nature* **555**, 231–236 (2018).

240 5.   Novoselov, K. S. *et al.* Two-dimensional atomic crystals. *Proc. Natl. Acad. Sci. U. S. A.* **102**, 10451–
241   10453 (2005).

242 6.   Wan, J. *et al.* Tuning two-dimensional nanomaterials by intercalation: Materials, properties and
243   applications. *Chemical Society Reviews* **45**, 6742–6765 (2016).

244 7.   Friend, R. H. & Yoffe, A. D. Electronic properties of intercalation complexes of the transition
245   metal dichalcogenides. *Adv. Phys.* **36**, 1–94 (1987).

246 8.   Wang, X., Shen, X., Wang, Z., Yu, R. & Chen, L. Atomic-scale clarification of structural transition of
247   MoS2 upon sodium intercalation. *ACS Nano* **8**, 11394–11400 (2014).

248 9.   Tan, S. J. R. *et al.* Chemical Stabilization of 1T' Phase Transition Metal Dichalcogenides with Giant
249   Optical Kerr Nonlinearity. *J. Am. Chem. Soc.* **139**, 2504–2511 (2017).

250 10. Kanetani, K. *et al.* Ca intercalated bilayer graphene as a thinnest limit of superconducting C6Ca.
251   *Proc. Natl. Acad. Sci. U. S. A.* **109**, 19610–19613 (2012).

252 11. Yang, J. *et al.* Ultrahigh-current-density niobium disulfide catalysts for hydrogen evolution. *Nat.*
253   *Mater.* (2019). doi:10.1038/s41563-019-0463-8

254 12. Cui, F. *et al.* Controlled Growth and Thickness-Dependent Conduction-Type Transition of 2D
255   Ferrimagnetic Cr2S3 Semiconductors. *Adv. Mater.* **32**, 1905896 (2020).

256 13. Mortazavi, M., Wang, C., Deng, J., Shenoy, V. B. & Medhekar, N. V. Ab initio characterization of
257   layered MoS2 as anode for sodium-ion batteries. *J. Power Sources* **268**, 279–286 (2014).

258 14. Fu, D. *et al.* Molecular Beam Epitaxy of Highly Crystalline Monolayer Molybdenum Disulfide on
259   Hexagonal Boron Nitride. *J. Am. Chem. Soc.* **139**, 9392–9400 (2017).

260 15. Chen, J. *et al.* Homoepitaxial Growth of Large-Scale Highly Organized Transition Metal
261   Dichalcogenide Patterns. *Adv. Mater.* **30**, 1704674 (2018).

262 16. Liao, M. *et al.* Twist angle-dependent conductivities across MoS2/graphene heterojunctions. *Nat.*
263   *Commun.* **9**, 4068 (2018).

264 17. Koski, K. J. *et al.* Chemical intercalation of zerovalent metals into 2D layered Bi2Se 3 nanoribbons.
265   *J. Am. Chem. Soc.* **134**, 13773–13779 (2012).

266 18. Guilmeau, E., Barbier, T., Maignan, A. & Chateigner, D. Thermoelectric anisotropy and texture of
267   intercalated TiS2. *Appl. Phys. Lett.* **111**, 133903 (2017).

268   19.   Wang, M. *et al.* Chemical intercalation of heavy metal, semimetal, and semiconductor atoms into
269   2D layered chalcogenides. *2D Mater.* **5**, 045005 (2018).

270   20.   Dungey, K. E., Curtis, M. D. & Penner-Hahn, J. E. Structural Characterization and Thermal Stability
271   of MoS2 Intercalation Compounds. *Chem. Mater.* **10**, 2152–2161 (1998).

272   21.   Gong, Y. *et al.* Spatially controlled doping of two-dimensional SnS2 through intercalation for
273   electronics. *Nat. Nanotechnol.* **13**, 294–299 (2018).

274   22.   Chen, Z. *et al.* Interface confined hydrogen evolution reaction in zero valent metal nanoparticles-
275   intercalated molybdenum disulfide. *Nat. Commun.* **8**, 14548 (2017).

276   23.   Liu, C. *et al.* Dynamic Ag+-intercalation with AgSnSe2 nano-precipitates in Cl-doped
277   polycrystalline SnSe2 toward ultra-high thermoelectric performance. *J. Mater. Chem. A* **7**, 9761–
278   9772 (2019).

279   24.   Bouwmeester, H. J. M., Van Der Lee, A., Van Smaalen, S. & Wiegers, G. A. Order-disorder
280   transition in silver-intercalated niobium disulfide compounds. II. Magnetic and electrical
281   properties. *Phys. Rev. B* **43**, 9431–9435 (1991).

282   25.   Wan, C. *et al.* Flexible n-type thermoelectric materials by organic intercalation of layered
283   transition metal dichalcogenide TiS2. *Nat. Mater.* **14**, 622–627 (2015).

284   26.   Jeong, S. *et al.* Tandem intercalation strategy for single-layer nanosheets as an effective
285   alternative to conventional exfoliation processes. *Nat. Commun.* **6**, 5763 (2015).

286   27.   O'Brien, E. S. *et al.* Single-crystal-to-single-crystal intercalation of a low-bandgap superatomic
287   crystal. *Nat. Chem.* **9**, 1170–1174 (2017).

288   28.   Kumar, P., Skomski, R. & Pushpa, R. Magnetically Ordered Transition-Metal-Intercalated WSe2.
289   *ACS Omega* **2**, 7985–7990 (2017).

290   29.   Kim, S. *et al.* Interstitial Mo-Assisted Photovoltaic Effect in Multilayer MoSe2 Phototransistors.
291   *Adv. Mater.* **30**, 1705542 (2018).

292   30.   Zhang, M. *et al.* Electron Density Optimization and the Anisotropic Thermoelectric Properties of
293   Ti Self-Intercalated Ti1+xS2 Compounds. *ACS Appl. Mater. Interfaces* **10**, 32344–32354 (2018).

294   31.   Wang, S. *et al.* Shape evolution of monolayer MoS2 crystals grown by chemical vapor deposition.
295   *Chem. Mater.* **26**, 6371–6379 (2014).

296   32.   Zhao, X. *et al.* Mo-Terminated Edge Reconstructions in Nanoporous Molybdenum Disulfide Film.
297   *Nano Lett.* **18**, 482–490 (2018).

298   33.   Mounet, N. *et al.* Two-dimensional materials from high-throughput computational exfoliation of
299   experimentally known compounds. *Nat. Nanotechnol.* **13**, 246–252 (2018).

300   34.   Azizi, A. *et al.* Spontaneous Formation of Atomically Thin Stripes in Transition Metal
301   Dichalcogenide Monolayers. *Nano Lett.* **16**, 6982–6987 (2016).

302   35.   Motome, Y., Furukawa, N. & Nagaosa, N. Competing Orders and Disorder-Induced Insulator to
303   Metal Transition in Manganites. *Phys. Rev. Lett.* **91**, 167204 (2003).

304   36.   Parish, M. M. & Littlewood, P. B. Non-saturating magnetoresistance in heavily disordered
305   semiconductors. *Nature* **426**, 162–165 (2003).

306   37.   Jiang, Z. *et al.* Structural and proximity-induced ferromagnetic properties of topological insulator-
307   magnetic insulator heterostructures. *AIP Adv.* **6**, 55809 (2016).

308   38.   Jiang, Z. *et al.* Independent Tuning of Electronic Properties and Induced Ferromagnetism in
309   Topological Insulators with Heterostructure Approach. *Nano Lett.* **15**, 5835–5840 (2015).

310   39.   Nagaosa, N., Sinova, J., Onoda, S., MacDonald, A. H. & Ong, N. P. Anomalous Hall effect. *Rev.*
311   *Mod. Phys.* **82**, 1539–1592 (2010).

312   40.   Zener, C. Interaction between the d shells in the transition metals. *Phys. Rev.* **81**, 440–444 (1951).

313   41.   Coelho, P. M. *et al.* Charge Density Wave State Suppresses Ferromagnetic Ordering in VSe2
314   Monolayers. *J. Phys. Chem. C* **123**, 14089–14096 (2019).

315   42.   Haastrup, S. *et al.* The Computational 2D Materials Database: High-throughput modeling and
316   discovery of atomically thin crystals. *2D Materials* **5**, 042002 (2018).

317   43.   Karthikeyan, J., Komsa, H.-P., Batzill, M. & Krasheninnikov, A. V. Which Transition Metal Atoms
318   Can Be Embedded into Two-Dimensional Molybdenum Dichalcogenides and Add Magnetism?
319   *Nano Lett.* **19**, 4581–4587 (2019).

320   44.   Wang, H. *et al.* High-quality monolayer superconductor NbSe2 grown by chemical vapour
321   deposition. *Nat. Commun.* **8**, 394 (2017).

322   45.   Enkovaara, J. *et al.* Electronic structure calculations with GPAW: A real-space implementation of
323   the projector augmented-wave method. *Journal of Physics Condensed Matter* **22**, 253202 (2010).

324   46.   Monkhorst, H. J. & Pack, J. D. Special points for Brillouin-zone integrations. *Phys. Rev. B* **13**, 5188–
325   5192 (1976).

326   47.   Perdew, J. P., Burke, K. & Ernzerhof, M. Generalized gradient approximation made simple. *Phys.*
327   *Rev. Lett.* **77**, 3865–3868 (1996).

328   48.   Wellendorff, J. *et al.* Density functionals for surface science: Exchange-correlation model
329   development with Bayesian error estimation. *Phys. Rev. B* **85**, 235149 (2012).

330

Acknowledgements

Author contributions

X. Z., S. J. P., and K. P. L. conceived the idea. S. J. P., and K. P. L. supervised the execution of the whole work. X. Z. performed the electron microscopy experiments and data analysis. X. L., A. C. R. and C. C. W. did the DFT calculation and data analysis. A. C. R-J. and K. S. T. performed the high-throughput DFT calculations. W. F., Y. D., and L. K. grew the samples. D. W. measured the magnetism. P. S. did device fabrication and measurement. J. D., and S. N. developed the python scripts for data analysis. All the authors discussed the results. All authors participated in writing the manuscripts. X. Z., and P. S. contributed equally to this work.

Competing interests

The authors declare no conflict of interest.

Additional information

**Supplementary information** is available for this paper at

Reprints and permissions information is available at www. nature.com/reprints.

Correspondence and requests for materials should be addressed to X. L., S. J. P. and K. P. L.

Publisher's note: Springer Nature remains neutral with regard to jurisdictional claims in published maps and institutional affiliations.

Main figure legends:

365
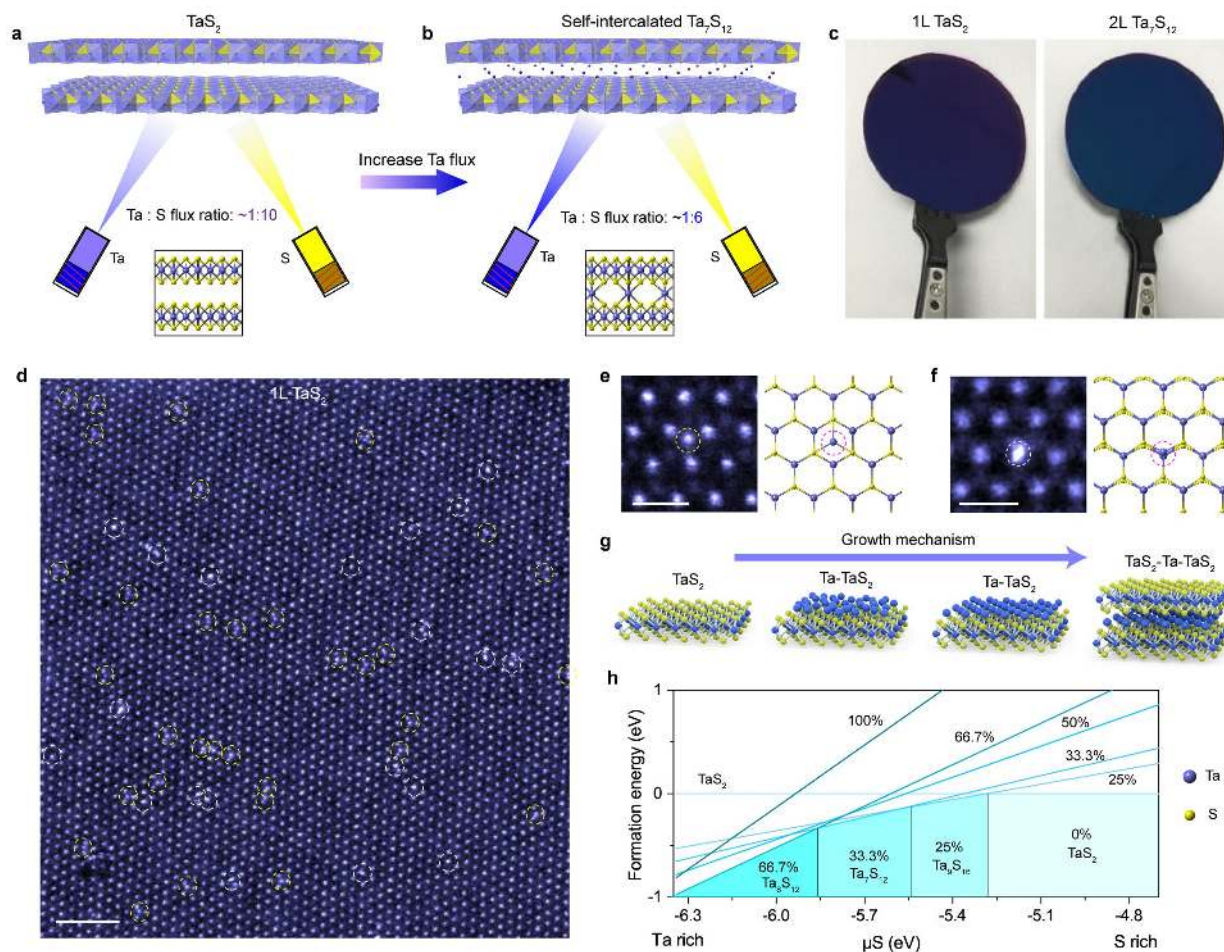
Figure 1. Self-intercalation in TaS₂ crystals. Schematic illustration showing the MBE growth of (a) pristine TaS$_2$ and (b) self-intercalated Ta$_7$S$_{12}$ under a low and high Ta-flux environment, respectively. The lower Ta flux produces stoichiometric TaS$_2$, whereas higher Ta flux leads to a self-intercalated phase. (c) Photographs of MBE-grown 1L-TaS$_2$ and 2L-Ta$_7$S$_{12}$ on 2-inch SiO$_2$/Si wafer. (d) Atomic-resolution STEM-ADF image of monolayer TaS$_2$ under Ta rich conditions with abundant Ta interstitials locating at the (e) center of honeycomb or (f) on top of the Ta site. Corresponding atomic models were depicted in the right panels. (g) Schematic illustration depicting the layer-by-layer growth of *ic*-2d crystals. (h) Calculated formation energies of various self-intercalated Ta$_x$S$_y$ phases where the intercalation concentrations are

25%, 33.3%, 50%, 66.7%, and 100%, respectively, as a function of sulfur chemical potential. Scale bars: 2

375 nm in (d); 0.5 nm in (e-f).

376
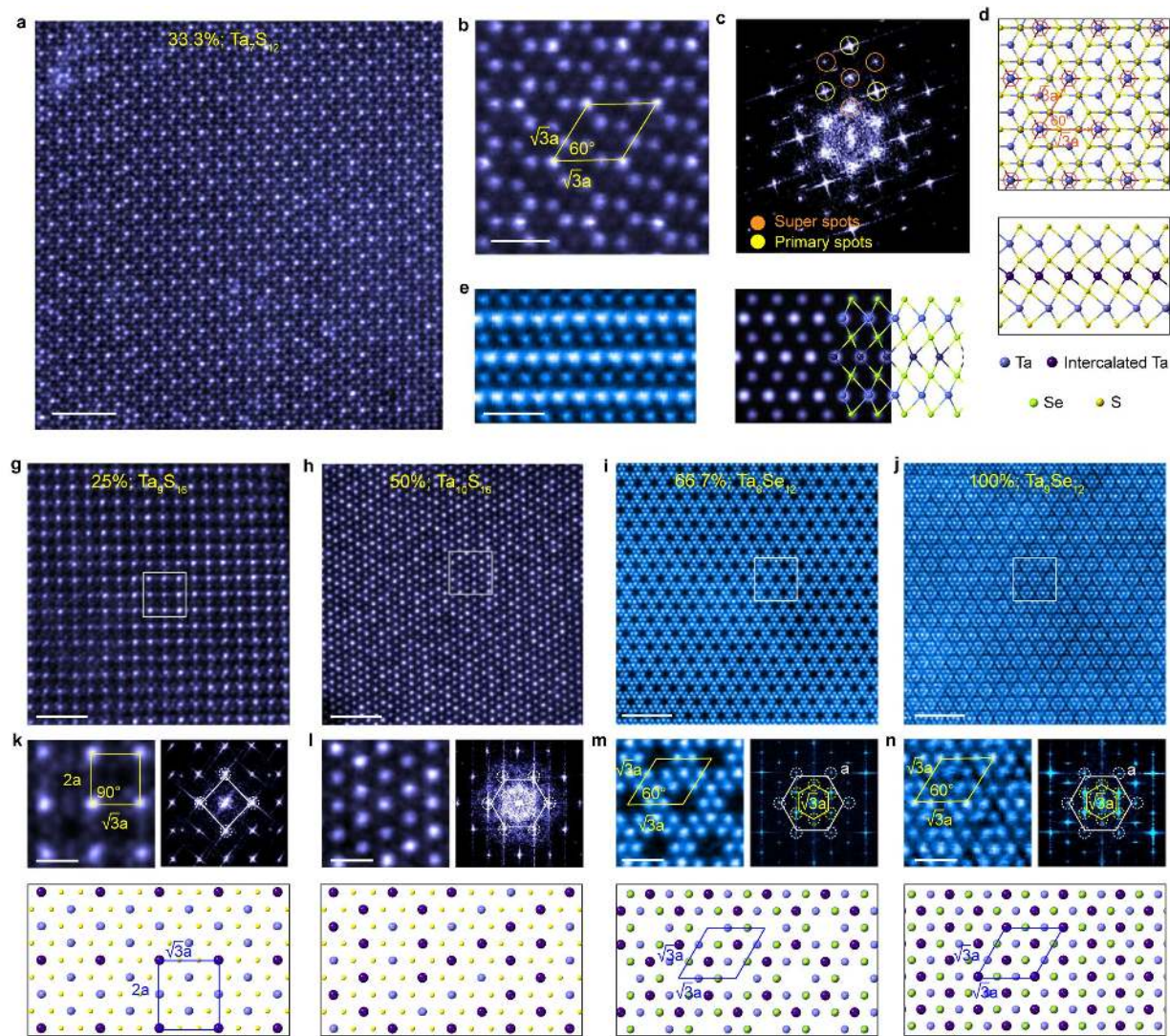
Figure 2. Compositional engineering of self-intercalated Ta_xS_y (Ta_xSe_y) with different intercalated Ta concentrations. (a) Atomic-resolution STEM-ADF image of the MBE grown self-intercalated Ta_7S_{12} showing well defined $\sqrt{3}a$ x $\sqrt{3}a$ superstructure and (b) the enlarged image overlaid with the atomic model. (c) corresponding FFT pattern of (a) with $\sqrt{3}a$ superspots highlighted by the orange circles. (d) Atomic model of self-intercalated Ta_7S_{12}. (e) STEM cross-section view of 100% Ta-intercalated $Ta_9Se_{12,}$ and

382   (f) its corresponding simulated image derived from the DFT optimized atomic model. Atomic-resolution

383   STEM images of (g) 25% self-intercalated Ta_9S_{16}, (h) 50% self-intercalated $Ta_{10}S_{16}$, (i) 66.7% self-

384   intercalated Ta_8Se_{12}, and (j) 100% self-intercalated Ta_9Se_{12} *ic*-2d crystals. (k-n) Enlarged white box regions

385   from (g-j), respectively, and their corresponding FFT patterns and atomic models are depicted in the right,

386   and lower panels, respectively. Scale bars: 2 nm in (a, g-j); 0.5 nm in (b, e, k-n).
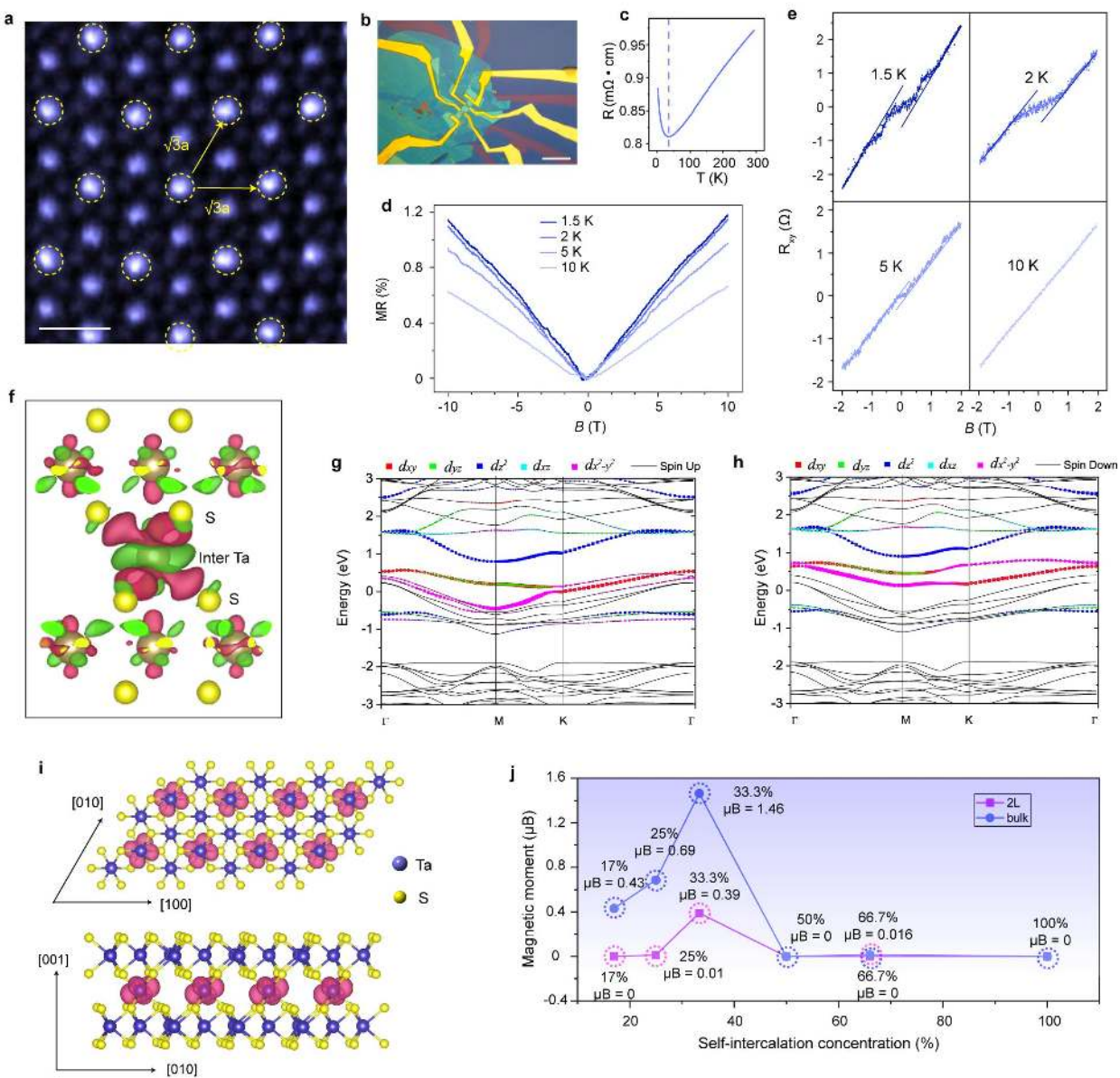
387

388   **Figure 3. Ferromagnetism in self-intercalated Ta$_7$S$_{12}$ *ic*-2d crystals**. (a) Atomic-resolution STEM-ADF

389   image of a typical self-intercalated Ta$_7$S$_{12}$ film. (b) Optical microscopy image of Ta$_7$S$_{12}$ Hall bar device

390   encapsulated with *h*-BN. (c) Resistivity as a function of temperature. Temperature dependent (d)

391   longitudinal resistance (R$_{xx}$) and (e) Hall resistance (R$_{xy}$) under the out-of-plane magnetic field. (f) Contour

392   plot of charge density difference in Ta-intercalated Ta$_7$S$_{12}$. Orbital-resolved (g) spin up and (h) spin down

393   band structures of Ta$_7$S$_{12}$. (i) Top view and the side view spin density isosurface of Ta-intercalated Ta$_7$S$_{12}$.

394   (j) Calculated magnetic moments as a function of Ta intercalation concentration in nonstoichiometric Ta$_x$S$_y$.

395   The STEM-ADF image shown in Fig. 3a was collected using a half-angle range from ~30 to 110 mrad to

396   enhance the contrast of S. Scale bar: 0.5 nm in (a); 20 μm in (b).
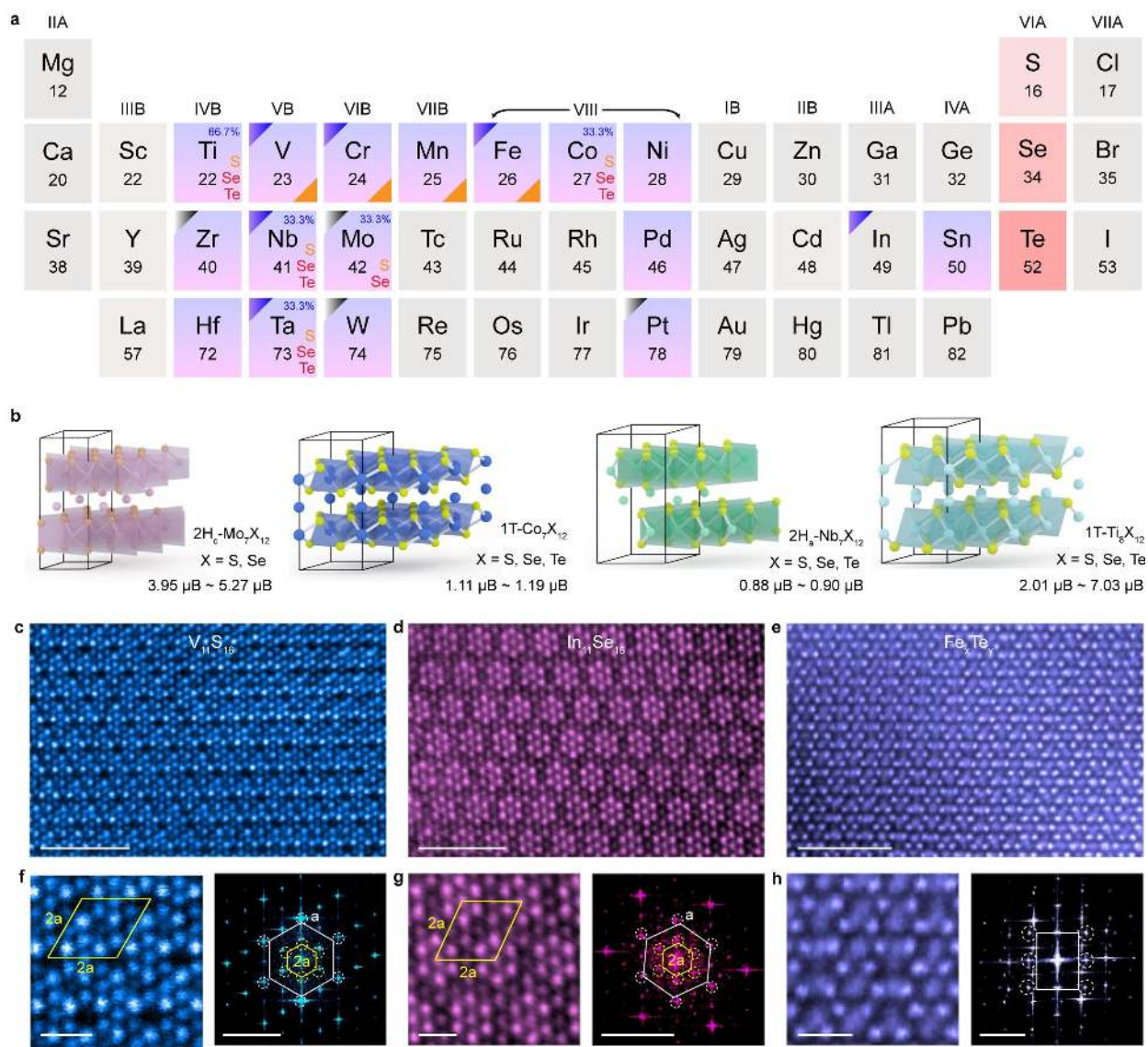
Figure 4. A library of *ic*-2d crystals. (a) Periodic table showing metal (highlighted blue) and chalcogen (highlighted red) combinations that form *ic*-2d crystals according to our DFT calculation; the list is non-exhaustive. Blue triangles indicate that the self-intercalation can be experimentally realized, whereas gray triangles indicate that intercalation was not successful under our experimental conditions. Intrinsic ferromagnetic MX_2 are highlighted by orange triangles. (b) DFT calculated *ic*-2d atomic models showing ferromagnetism. STEM-ADF images of self-intercalated (c) $V_{11}S_{16}$, (d) $In_{11}Se_{16}$, and (e) Fe_xTe_y. Their

404   enlarged images and corresponding FFT patterns are depicted in (f-h), respectively. 2 nm in (c-e); 0.5 nm

405   in (f-h); 5 nm^{-1} for all FFT patterns in (f-h).

Methods

MBE growth of self-intercalated TMD films. *Ta-intercalated Ta$_x$S$_y$* films were grown in a dedicated MBE

408   chamber (base pressure < 6×10^{-10} torr). Prior to the growth, the 2-inch SiO$_2$ substrates were degassed in

409   the same chamber at 500 °C for 2 h. Ultrapure Ta (99.995%, Goodfellow) and S powders (99.5% Alfa Aesar)

410   were evaporated from a mini electron-beam evaporator and a standard sulphur valved cracker,

411   respectively. The flux density of Ta was precisely controlled by adjusting the flux current. The S cracker

412   cell temperature was maintained at 110 °C, and the flux density was controlled by the shutter of the

413   cracker valve. The substrate temperature was maintained at 600 to 650 °C and the growth time is about

414   3 hours for all thin films. 25% Ta-intercalated Ta$_9$S$_{16}$, 33.3% Ta$_7$S$_{12}$, and 50% Ta$_{10}$S$_{16}$ films were controlled

415   grown when the Ta/S ratio is set as ~1:8, ~1:6, and ~1:5, respectively. A slightly higher growth temperature

416   will facilitate the self-intercalation process. After growth, both sources were turned off and the sample

417   was further annealed for another 30 mins before cooling down to the room temperature. ***In-intercalated***

418   ***In$_x$Se$_y$*** were grown in a customized MBE chamber (base pressure < 6×10^{-10} torr). Prior to growth, the 1 cm

419   × 1 cm SiO$_2$ substrate was degassed in the chamber at 600 °C for 1 h. Ultrapure In$_2$Se$_3$ powder (99.99%)

420   and Se pellets (99.999%) were evaporated from a mini electron-beam evaporator and an effusion cell,

421   respectively. The Se effusion-cell temperature was set at 150 °C with a hot-lip at 220 °C. The substrate

422   temperature was maintained at 400 °C and the growth time is about 2 hours. In$_{11}$Se$_{16}$ films were controlled

423   grown when the In$_2$Se$_3$/Se ratio is set as ~1:3.

CVD growth of self-intercalated TMD films. *Ta-intercalated Ta$_x$Se$_y$* crystals were grown by CVD. Prior to

425   the growth, the SiO$_2$ substrate was sequentially cleaned by water and acetone, followed by 5 min of O$_2$

426   plasma. The furnace was purged by 300 sccm Ar gas for 5 mins. Se powders and mixed Ta/TaCl$_5$ powders

427   were applied as precursors that were located upstream in a one-inch quartz tube. 40 sccm Ar and 10 sccm

428   H$_2$ were used as a carrier gas. The samples were grown at 800 °C for 30 mins. After growth, the sample

429   was cooled down quickly in a continuous stream of Ar. 66.7% Ta-intercalated Ta$_8$Se$_{12}$, and 100% Ta-

430   intercalated Ta$_9$Se$_{12}$ were controlled grown when the Se powders and mixed Ta/TaCl$_5$ powders are 1 g/15

431   mg/1.5 mg, and 1 g/30 mg/3 mg, respectively. ***V-intercalated V$_x$S$_y$*** crystals were grown by CVD. Prior to

432   the growth, the SiO$_2$ substrates were treated by the same method as indicated in growing Ta$_x$Se$_y$. Two

433   quartz boats containing 0.5 g S, and 0.3 g VCl$_3$ were loaded in the upstream of the one-inch quartz tube

434   serving as precursors. Carrier gases were 40 sccm Ar together with 10 sccm H$_2$. The sample was grown at

435   680 °C for 30 mins. After growth, the sample was cooled down quickly under the protection of 100 sccm

436   Ar. ***Fe-intercalated Fe$_x$Te$_y$*** crystals were grown by CVD. Prior to the growth, the SiO$_2$ substrates were

437   treated by the same method as indicated in growing Ta$_x$Se$_y$. Two quartz boats containing Te (>99.997%)

438   and FeCl$_2$ (>99.9%) were placed in the upstream in sequence of the one-inch quartz tube serving as

439   precursors. The sample was grown at 600 °C for 30 mins. After growth, the sample was cooled down

440   quickly under the protection of 100 sccm Ar.

441   **Sample characterization.** XPS was performed using SPECS XR 50 X-ray Al Kα (1486.6eV) source with a pass

442   energy of 30 eV. The chamber base pressure is lower than 8 × 10^{-10} mbar. Raman spectra were collected

443   at room temperature using the confocal WiTec Alpha 300R Raman Microscope (laser excitation: 532 nm).

444   **STEM sample preparation, image characterization, and image simulation.** The as-grown TMD films were

445   transferred *via* a PMMA method under the protection of graphene. Continuous graphene film was coated

446   on fresh Ta$_7$S$_{12}$ film to protect the surface oxidation *via* conventional PMMA method. Subsequently,

447   graphene/Ta$_7$S$_{12}$ composites were immersed in 1 M KOH solution to detach the PMMA/ Ta$_7$S$_{12}$ composite

448   from the SiO$_2$ substrate, followed by rinsing in DI water. The PMMA/graphene/Ta$_7$S$_{12}$ film was then placed

449   onto Cu quantifoil TEM grid which was precoated with continuous graphene film[44]. The TEM grid was then

450   immersed in acetone to remove the PMMA films. Atomic-resolution STEM-ADF imaging was performed

451   on an aberration-corrected ARM200F, equipped with a cold field-emission gun and an ASCOR corrector

452   operating at 60 kV. The STEM-ADF images were collected using a half-angle range from ~81 to 280 mrad

453   unless indicated elsewhere. The convergence semiangle of the probe was ~30 mrad. Image simulations

454   were done with the QSTEM package assuming an aberration-free probe with a probe size of ≈1 Å. The

455   convergence semiangle of the probe was set as ~30 mrad, and the accelerating voltage is 60 kV in line

456   with the experiments. The collection angle for HAADF and MAADF images were from 81 to 280 mrad and

457   30 to 110 mrad, respectively. The thermal diffuse scattering (TDS) was set as 30 with defocus value 0. The

458   STEM-EDS were collected and processed in an Oxford Aztec EDS system

459   **Device fabrication and measurements.** MBE-grown Ta_7S_{12} and CVD-grown Ta_8Se_{12} were selected to

460   fabricate Hall-bar devices using e-beam lithography and e-beam evaporation of Ti/Au (2/60 nm). The MBE-

461   grown Ta_7S_{12} film was then etched into Hall-bar geometry using deep reactive ion etching. The final

462   devices were encapsulated with h-BN flakes using a dry-transfer method in the glovebox (both O_2 and H_2O

463   less than 1 ppm), to avoid degradation of Ta_7S_{12} and Ta_8Se_{12} under ambient conditions. Low-temperature

464   Transport measurements were carried out in Oxford Teslatron system. All resistances were derived from

465   four-terminal measurements using SR830 lock-in amplifier, with constant excitation current of 1 μA.

466   **DFT calculations.** First-principles calculations based on Density Functional Theory (DFT) were

467   implemented in the plane wave code VASP using the projector-augmented wave (PAW) potential

468   approach. For the exchange and correlation functional, both the local density approximation (LDA) and

469   the PBE flavor of the generalized gradient approximation are used and found no significant differences in

470   the results. A kinetic energy cutoff of 500 eV is used for the TaS_2. A Monkhorst Pack k-grid samplings with

471   a k-point density of 6.0 $Å^{-1}$ were used for geometry optimization. For thin-film calculations, a vacuum

472   thickness of 20 Å is added in the slab to minimize the interaction between adjacent image cells. Geometry

473   optimization was performed with the maximum force convergence criterion of 0.005 eV/ Å. To treat the

474   strong on-site Coulomb interaction of localized Ta-d orbitals, we use Dudarev's approach with an effective

475   U parameter of U_{eff}=3.0 eV. The zone center phonon modes were calculated by using the density

476   functional perturbation theory (DFPT) with the local density approximation functionals. **High-throughput**

477   **DFT calculations** were carried out with the electronic structure code GPAW[45] following a semi-automated

478   workflow for maximal consistency and accuracy[42]. The relaxations of the self-intercalated bilayers are

479   done on a Monkhorst-Pack[46] grid with a k-point density of 6.0 Å^{-1} using the PBE[47] and BEEF-vdW

480   functionals[48] for describing exchange-correlation effects. 15 Å vacuum is used in the out-of-plane direction

481   to avoid non-physical periodic interactions. The plane-wave expansion is cut-off at 800 eV. All systems are

482   relaxed until the maximum force on any atom is 0.01 eV/Å and the maximum stress on the unit cell is

483   0.002 eV/ Å^{-3}. All systems are calculated in the intercalated structure with both a spin-paired calculation

484   and a spin-polarized calculation. If the total energy of the spin-polarized structure is found to be over 0.01

485   eV/atom lower than the spin-paired structure, the structure is concluded to be magnetically more stable

486   than its non-magnetic counterpart. The atomic structures of calculated self-intercalated TMDs (33.3% and

487   66.7% intercalation concentration) were presented in Supplementary Fig. 29, in which the polymorphism

488   of single layer MoX_2, WX_2, NbX_2, and TaX_2 (X = S, Se, and Te) reveals an H-phase, whereas the rest TMDs

489   are T-phase taking an *AA* stacking polytype. MoX_2, and WX_2 comply the *AA'* stacking order whereas NbX_2,

490   and TaX_2 take the *AB'* stacking registry. All intercalants occupy the octahedral vacancies in the vdW gap.

491   **Method references:**

492   42.   Haastrup, S. *et al.* The Computational 2D Materials Database: High-throughput modeling and
493   discovery of atomically thin crystals. *2D Materials* **5**, 042002 (2018).

494   44.   Wang, H. *et al.* High-quality monolayer superconductor NbSe2 grown by chemical vapour
495   deposition. *Nat. Commun.* **8**, 394 (2017).

496   45.   Enkovaara, J. *et al.* Electronic structure calculations with GPAW: A real-space implementation of
497   the projector augmented-wave method. *Journal of Physics Condensed Matter* **22**, 253202 (2010).

498   46.   Monkhorst, H. J. & Pack, J. D. Special points for Brillouin-zone integrations. *Phys. Rev. B* **13**, 5188–
499   5192 (1976).

500   47.   Perdew, J. P., Burke, K. & Ernzerhof, M. Generalized gradient approximation made simple. *Phys.
501   Rev. Lett.* **77**, 3865–3868 (1996).

502   48.   Wellendorff, J. *et al.* Density functionals for surface science: Exchange-correlation model
503   development with Bayesian error estimation. *Phys. Rev. B* **85**, 235149 (2012).

504   **Data availability.** The main data supporting the findings of this study are available within the paper and

505   its Supplementary Information. Extra data are available from the corresponding authors upon request.